Journal of Sound and Vibration (1998) **213**(4), 709–737

THE MECHANICS OF HIGHLY-EXTENSIBLE CABLES

A. A. TJAVARAS,† Q. ZHU, Y. LIU, M. S. TRIANTAFYLLOU‡ AND D. K. P. YUE

Department of Ocean Engineering, *Massachusetts Institute of Technology*, *Cambridge*, *MA* 02139, *U.S.A.*

(*Received* 7 *July* 1997, *and in final form* 26 *January* 1998)

The mechanics of highly extensible cables are studied numerically. The governing equations for the cable motion are reformulated using Euler parameters and we employ a non-linear stress–strain relation. Also, bending–stiffness terms are included to ensure a well-posed problem when tension becomes very low. Thus, the singularity associated with Euler–angle formulation is removed and the model allows for shock formation, while it can accommodate zero or negative tension along the cable span. Implicit time integration and non-uniform grid along the cable are adopted for the numerical solution of the governing equations. The model is employed to investigate (1) the dynamical behaviour of the breaking and post-breaking of an initially taut cable; and (2) the dynamic response of a tethered near-surface buoy subject to wave excitation. For a breaking cable we find that the speed of snapback, which can have potentially catastrophic effects, is proportional to the initial strain level, but the principal parameter controlling the cable behaviour is the time it takes for the cable to fracture. In the case of a tethered buoy in waves, we find that beyond a threshold wave amplitude the system begins to exhibit first zero tension, then followed by snapping response, while the buoy performs chaotic motion.

1. INTRODUCTION

The mechanics of extensible cables that have a linear stress–strain relation, as well as the mechanics of inextensible chains, in air and in water, have been the object of substantial research [1, 2]. More recently, the mechanics of cables under low or zero tension, situations that are often encountered in the umbilical tethers of remotely operated vehicles (ROV), have been considered. The problems arising in regions of low tension and the way to address them are discussed in the work of Dowling [3], Triantafyllou and Triantafyllou [4], Burgess [5], and Triantafyllou and Howell [6, 7].

Experimental methods have also been used to determine the breaking strength of synthetic lines and how it is affected by various factors such as rope construction, wet or dry condition, and cyclic loading. Bitting [8] determined that the dynamic stiffness of a synthetic line is larger than its quasi-static stiffness. Leeuwen [9], Flory [10] and Shin *et al*. [11] performed several similar experiments and found that the stress–strain relation of synthetic lines is visco-elastic when the lines are new. The parameters of the stress–strain relation seem to depend on the type of loading and also to vary during the life of the line. In general, the visco-elastic effects get attenuated by prolonged use of the line and the stress–strain relation settles to an expression which is non-linear but with weak memory effects.

---

† Currently with Exxon Production Research Co., Houston, Texas, U.S.A.

‡ Corresponding author.

0022–460X/98/240709 + 29 $25.00/0/sv981526

In a more recent effort, Bitting [12] used experiments to determine the coefficients of a visco-elastic model known as the *standard linear solid model* [13]. Recently, Triantafyllou and Yue [14] used analytical methods to investigate the effects of the hysteretic character of the stress–strain relation of synthetic cables on the damping of their transverse motion.

In this work we develop a set of equations describing the motion of a highly-extensible cable, using Euler parameters to represent the relative rotation of the reference frames to avoid the singularity accompanying the Euler–angle representation. The bending stiffness of the cable is included to avoid an ill-posed problem when the tension becomes small [15]. Finally an arbitrary tension–strain relation is allowed.

An implicit numerical integration scheme is used, which allows long-term simulation with small overall error. To demonstrate the applications of this method, we studied two problems: the post-breaking behaviour of a synthetic cable and the dynamic response of a moored near-surface buoy in surface waves.

The problem of a breaking synthetic cable is significant because for the same external load a highly extensible cable stores a much larger potential energy than a wire rope; this can have catastrophic effects. Research on this subject has been so far mainly experimental. Feyrer [16] conducted an experimental study of the snapback of synthetic cables using long lines; hence he had to conduct his experiments outdoors. The motion of the breaking line was filmed and measurements were made from the film, which provide qualitative, rather than quantitative results of the motion of the line, due to the high speed of response. Bitting [17] conducted similar experiments but he used shorter specimens and thus was able to conduct his experiments in the laboratory. As a result, his measurements of the position of the line at each frame are obtained more accurately. Paul [18] used analytic energy calculations to determine the length and strength of synthetic ropes that can be safely used to stop moving objects. He also used energy calculations to determine the snap-back velocity of breaking lines. Whereas experimental results are difficult to quantify due to the high speed response of the line, the numerical capability presented herein captures the dynamic response very accurately and allows the study of the principal mechanisms involved.

Tethered buoys are used extensively for oceanographic applications and for mooring ships and floating structures. Grosenbaugh [19] addressed the problem of oceanographic buoys with very long tethers, where an equivalent linearization of the drag force can produce valuable information on the wave-induced dynamic tensions. Idris *et al*. [20] addressed the problem of moored buoys using numerical simulation. The problem of the motion of a underwater buoy tethered by cable to the bottom involves long-term simulation of cable dynamics, which is possible under the present formulation, which uses Euler parameters and an implicit time integration schemes.

2. PHYSICAL PROBLEM AND MATHEMATIC FORMULATION

We consider the dynamical behaviour of a highly-extensible cable. To derive the equations of motion, we assume that: (1) at least piece-wise the cross-section of the cable is homogeneous and circular or annular; (2) the Euler–Bernoulli beam model represents adequately the effects of bending; (3) the tension is a single-valued function of the strain. The partial differential equations of the cable motion are derived by considering the balance of forces, the balance of moments and the compatibility relation for a cable segment of infinitesimal length. The stress–strain relation is not necessarily linear but can be any single-valued function. The fluid forces due to a current varying both in space and time are taken into account.

2.1. ROTATION MATRIX

We define two coordinate systems: (X, Y, Z) is a space-fixed rectangular coordinate system with unit vectors $\hat{\imath}$, $\hat{\jmath}$ and $\hat{k}$; (x, y, z) is a local, Lagrangian reference frame with unit vectors $\hat{t}$, $\hat{n}$ and $\hat{b}$, where $\hat{t}$ points in the direction of the local tangent of the cable, $\hat{n}$ in the direction of the maximum curvature (normal direction), and $\hat{b}$ in the bi-normal direction. Next, it is necessary to obtain the transformation matrix between systems. The unit vectors of the local reference frame $\hat{t}$, $\hat{n}$ and $\hat{b}$ can be written as linear combinations of the unit vectors of the fixed reference frame $\hat{\imath}$, $\hat{\jmath}$ and $\hat{k}$:

$$\begin{bmatrix} \hat{t} \\ \hat{n} \\ \hat{b} \end{bmatrix} = \mathbf{C} \begin{bmatrix} \hat{\imath} \\ \hat{\jmath} \\ \hat{k} \end{bmatrix}. \tag{1}$$

Here the matrix $\mathbf{C}$, called the *rotation matrix*, varies both along the cable span and with time, i.e. $\mathbf{C} = \mathbf{C}(s, t)$.

Since the length of the cable is several orders of magnitude larger than its diameter, its configuration and motion can be described by the shape and motion of its centreline. We tag each point along the cable with the distance s from the end of the cable to this point when the cable is not stretched. Considering an arbitrary vector $\mathbf{G} = \mathbf{G}(s, t)$, $\mathbf{G} = [G_X, G_Y, G_Z]$ in the fixed reference frame. Going to the local reference frame, $\mathbf{G} = [G_1, G_2, G_3]$. These two expressions of $\mathbf{G}$ are linked by the rotation matrix

$$\begin{bmatrix} G_1 \\ G_2 \\ G_3 \end{bmatrix} = \mathbf{C} \begin{bmatrix} G_X \\ G_Y \\ G_Z \end{bmatrix}. \tag{2}$$

We denote the angular velocity of the local reference frame with respect to the fixed reference frame by $\omega(s, t)$ and the Darboux vector of the cable by $\Omega(s, t)$, then the derivatives of $\mathbf{G}$ are given by

$$\frac{\mathrm{D}\mathbf{G}}{\mathrm{D}t} = \frac{\partial \mathbf{G}}{\partial t} + \omega \times \mathbf{G}, \qquad \frac{\mathrm{D}\mathbf{G}}{\mathrm{D}s} = \frac{\partial \mathbf{G}}{\partial s} + \Omega \times \mathbf{G}. \tag{3, 4}$$

Note that the Darboux vector $\Omega(s, t)$ is defined as in Landau and Lifshitz [21], i.e. the torsion is the material torsion of the cable and not the geometric torsion of the line.

The most commonly used method to obtain the rotation matrix $\mathbf{C}$ is using three Euler angles. Its disadvantage is a well-known singularity involved in Euler–angle methods. The standard way to avoid it is to choose a sequence of rotations which become singular at a position that we do not expect to occur. However, for long-time simulations, in which the range of the motions can not be known in advance, the Euler–angle method is not adequate.

An alternative method of describing the rotation from fixed to Lagrangian frames is the method using Euler parameters, which shows no singularity. The method was first used in cables by Hover [22], and is based on the *principal rotation theorem* derived by Euler: an arbitrary orientation change can be achieved by a single rotation through a principal angle α about a principal unit vector $\hat{l}$. The four Euler parameters are defined in terms of α and components of $\hat{l}$:

$$\beta = \begin{bmatrix} \beta_0 \\ \beta_1 \\ \beta_2 \\ \beta_3 \end{bmatrix} = \begin{bmatrix} \cos(\alpha/2) \\ l_X \sin(\alpha/2) \\ l_Y \sin(\alpha/2) \\ l_Z \sin(\alpha/2) \end{bmatrix} \tag{5}$$

in terms of which, the rotation matrix can be written in the form:

$$\mathbf{C} = \begin{bmatrix} \beta_0^2 + \beta_1^2 - \beta_2^2 - \beta_3^2 & 2(\beta_1\beta_2 + \beta_0\beta_3) & 2(\beta_1\beta_3 - \beta_0\beta_2) \\ 2(\beta_1\beta_2 - \beta_0\beta_3) & \beta_0^2 - \beta_1^2 + \beta_2^2 - \beta_3^2 & 2(\beta_2\beta_3 + \beta_0\beta_1) \\ (\beta_1\beta_3 + \beta_0\beta_2) & 2(\beta_2\beta_3 - \beta_0\beta_1) & \beta_0^2 - \beta_1^2 - \beta_2^2 + \beta_3^2 \end{bmatrix}. \tag{6}$$

2.2. EQUATIONS OF MOTION

We study the motion of an infinitesimal segment of the cable of initial unstretched lengths ds, centred at a point s in a position $\mathbf{R}(s, t)$, as shown in Figure 1. Under the applied internal and external forces and moments, the segment stretches to a length ds_1. The strain $\varepsilon(s, t)$ is defined as

$$\varepsilon(s, t) = \frac{\mathrm{d}s_1 - \mathrm{d}s}{\mathrm{d}s}. \tag{7}$$

The velocity of the cable at s is

$$\mathbf{V}(s, t) = u\hat{t} + v\hat{n} + w\hat{b} = U\hat{i} + V\hat{j} + W\hat{k} = \frac{\partial \mathbf{R}}{\partial t}. \tag{8}$$

Because of stretching, the mass per unit length of the cable segment m is reduced to m_1. Using the principle of conservation of mass, the relation between m and m_1 is

$$m_1 = m\frac{\mathrm{d}s}{\mathrm{d}s_1}. \tag{9}$$

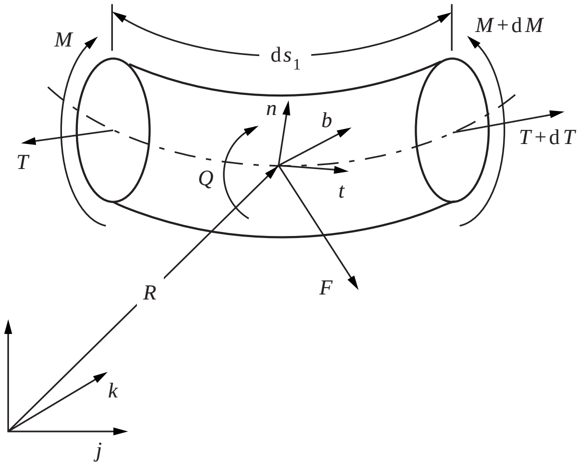

Figure 1. Cable segment used for the derivation of the cable equations.

For synthetic cables, the Poisson ratio is $\nu \approx 0{\cdot}5$ and the volume of the cable segment is conserved. Then

$$A_1 = A\frac{\mathrm{d}s}{\mathrm{d}s_1} = \frac{A}{1+\varepsilon}, \tag{10}$$

where A and A_1 are the cross-sectional areas before/after stretching.

The forces acting on the cable segment under consideration are: the internal force $\mathbf{T}$ ($\mathbf{T} = T\hat{t} + S_n\hat{n} + S_b\hat{b}$), and the external forces. If the cable is immersed in water, the external forces include the hydrostatic force, the hydrodynamic force and the gravity force. Applying Newton's second law, we obtain

$$m_1\frac{\mathrm{D}\mathbf{V}}{\mathrm{D}t} = \frac{\mathrm{D}\mathbf{T}}{\mathrm{D}s_1} + \mathbf{F}_e, \tag{11}$$

where $\mathbf{F}_e$ denotes the total external forces per unit length. Expanding the total derivative terms and making use of the mass conservation (9), we have

$$m\left(\frac{\partial\mathbf{V}}{\partial t} + \omega \times \mathbf{V}\right) = \frac{\partial\mathbf{T}}{\partial s} + \Omega \times \mathbf{T} + (1+\varepsilon)\mathbf{F}_e. \tag{12}$$

The moments acting on the cable segment under consideration are the internal moment $\mathbf{M} = M_\tau\hat{t} + M_n\hat{n} + M_b\hat{b}$ and the external moment $\mathbf{Q}$. Here,

$$M_\tau = GI_p\Omega_1, \qquad M_n = EI\Omega_2, \qquad M_b = EI\Omega_3, \tag{13–15}$$

where EI is the bending stiffness and GI_p the torsional stiffness of the cable. Since cables are not designed to sustain any external moments, $\mathbf{Q}$ is neglected. The moment equations are given by the balance of the internal moment and the moment caused by the internal force $\mathbf{T}$:

$$\frac{1}{(1+\varepsilon)^2}\frac{\partial\mathbf{M}}{\partial s} + \frac{1}{(1+\varepsilon)^2}\Omega \times \mathbf{M} + (1+\varepsilon)\hat{t} \times \mathbf{T} = 0. \tag{16}$$

For the configuration of the cable to be continuous, we must enforce the compatibility relation. The vector $\mathbf{R}(s, t)$ and its partial derivatives are continuous in t and s. This leads to

$$\frac{\mathrm{D}}{\mathrm{D}t}\left(\frac{\mathrm{D}\mathbf{R}}{\mathrm{D}s}\right) = \frac{\mathrm{D}}{\mathrm{D}s}\left(\frac{\mathrm{D}\mathbf{R}}{\mathrm{D}t}\right) \tag{17}$$

which can be rewritten as

$$\frac{\mathrm{D}}{\mathrm{D}t}[(1+\varepsilon)\hat{t}] = \frac{\mathrm{D}\mathbf{V}}{\mathrm{D}s} \tag{18}$$

after using the relation $\hat{t} = \partial\mathbf{R}/\partial s_1 = \partial\mathbf{R}/\partial s/(1+\varepsilon)$. Expanding the total derivatives, we obtain

$$\frac{\partial\varepsilon}{\partial t}\hat{t} + (1+\varepsilon)\omega \times \hat{t} = \frac{\partial\mathbf{V}}{\partial s} + \Omega \times \mathbf{V}. \tag{19}$$

At any point along the cable, the tension T and the strain ε are related by the tension–strain relation:

$$T = f(\varepsilon), \tag{20}$$

where the form of f depends on the properties of the cable.

In summary, we write the equations of motion in a vector form:

$$\frac{\partial \mathbf{Y}}{\partial s} + \mathbf{M}(\mathbf{Y})\frac{\partial \mathbf{Y}}{\partial t} + \mathbf{P}(\mathbf{Y}) = 0, \tag{21}$$

where

$$\mathbf{Y} = [\varepsilon \quad S_n \quad S_b \quad u \quad v \quad w \quad \beta_0 \quad \beta_1 \quad \beta_2 \quad \beta_3 \quad \Omega_1 \quad \Omega_2 \quad \Omega_3]^T \tag{22}$$

and the forms of **M** and **P** are shown in Appendix A.

2.3. HYDRODYNAMIC FORCES

The case of an immersed cable needs special attention. The hydrostatic force along a short portion of the cable span acts in the normal direction. To recover the buoyancy force, we hence add and subtract the missing pressure forces at the (imaginary) cuts at the ends of the infinitesimal section. As a result, we obtain the buoyancy force acting vertically, but the tension must be modified and becomes the effective tension $T_e = T + p_e A_1$ [23], where p_e is the hydrostatic pressure. The resulting buoyancy and gravity forces act in the vertical direction, and we hence combine them to form the net weight-in-water force $\mathbf{F}_w$:

$$(1+\varepsilon)\mathbf{F}_w = -w_0\hat{k}, \tag{23}$$

where $w_0 = mg - A\rho_w g$, ρ_w is the density of water and g the gravitational acceleration. The external force $\mathbf{F}_e$ can be separated into a static part $\mathbf{F}_w$ and a hydrodynamic part $\mathbf{F}_d$. In this paper we will always refer to the effective tension; hence the subscript e will be neglected.

Let the velocity of the water be $\mathbf{V}_c = u_c\hat{t} + v_c\hat{n} + w_c\hat{b} = U_c\hat{i} + V_c\hat{j} + W_c\hat{k}$; then the hydrodynamic force $\mathbf{F}_d$ is estimated using Morison's equation to be given by

$$\begin{aligned}(1+\varepsilon)\mathbf{F}_d = {} & -\tfrac{1}{2}\rho_w d\pi C_{dt}(u-u_c)|u-u_c|(1+\varepsilon)^{1/2}\hat{t} \\ & - \left[\frac{1}{2}\rho_w d C_{dp}(v_r^2 + w_r^2)^{1/2} v_r (1+\varepsilon)^{1/2} + \rho_w \frac{\pi d^2}{4}\dot{v}_c + m_a(\dot{v}_c - \dot{v})\right]\hat{n} \\ & - \left[\frac{1}{2}\rho_w d C_{dp}(v_r^2 + w_r^2)^{1/2} w_r (1+\varepsilon)^{1/2} + \rho_w \frac{\pi d^2}{4}\dot{w}_c + m_a(\dot{w}_c - \dot{w})\right]\hat{b},\end{aligned} \tag{24}$$

where $\dot{v}$, $\dot{w}$, $\dot{v}_c$, and $\dot{w}_c$ are the accelerations, $v_r = v - v_c$ and $w_r = w - w_c$ the relative velocities, m_a the added mass of the cable per unit length, d the diameter of the cable, C_{dt} and C_{dp} the drag coefficients in the tangential and normal directions, respectively. In our numerical study, $C_{dt} = 0{\cdot}1$ and $C_{dp} = 1{\cdot}0$ are chosen.

3. NUMERICAL METHOD

A finite-difference scheme, the so-called box method, is employed to solve the governing equations (21) for the cable motion. With this method, the implicit scheme is used for time integration. According to Wendroff [24], the box method has an accuracy of second order both in space and time and is unconditionally stable and convergent.

In implementation, the cable is divided into $n_p - 1$ discrete segments by means of n_p computational points ($k = 1, 2, \ldots, n_p$). Each segment has an unstretched length $\Delta s(k)$ defined as the length of the segment between the grid points k and $k+1$. The segment length is not necessarily constant along the cable. This allows us to have finer grids at the ends of the cable where the unknowns possess larger variations.

At each moment t_i, given the values of unknown variables ($\mathbf{Y}_{k,i-1}$) at the previous time step $t_{i-1} = t_i - \Delta t$, we need to determine the values of the unknown variables ($\mathbf{Y}_{k,i}$). To do that, we write the discrete form of the governing equations (21) at the centre of each computational "box".

At the centre of the "box", we approximate the value of the unknown $\mathbf{Y}_{k-1/2,i-1/2}$ by

$$\mathbf{Y}_{k-1/2,i-1/2} \rightarrow \tfrac{1}{4}(\mathbf{Y}_{k-1,i-1} + \mathbf{Y}_{k-1,i} + \mathbf{Y}_{k,i-1} + \mathbf{Y}_{k,i}) \tag{25}$$

and the time and space derivatives of the unknown by

$$\left(\frac{\partial \mathbf{Y}}{\partial t}\right)_{k-1/2,i-1/2} \rightarrow \frac{1}{2}\left(\frac{\mathbf{Y}_{k-1,i} - \mathbf{Y}_{k-1,i-1}}{\Delta t} + \frac{\mathbf{Y}_{k,i} - \mathbf{Y}_{k,i-1}}{\Delta t}\right), \tag{26}$$

$$\left(\frac{\partial \mathbf{Y}}{\partial s}\right)_{k-1/2,i-1/2} \rightarrow \frac{1}{2}\left(\frac{\mathbf{Y}_{k,i-1} - \mathbf{Y}_{k-1,i-1}}{\Delta s(k-1)} + \frac{\mathbf{Y}_{k,i} - \mathbf{Y}_{k-1,i}}{\Delta s(k-1)}\right). \tag{27}$$

The resulting discrete approximation of the governing equations (21) at the point $(k-1/2, i-1/2)$ takes the form:

$$\begin{aligned} &2\Delta t(\mathbf{Y}_{k,i} - \mathbf{Y}_{k-1,i} + \mathbf{Y}_{k,i-1} - \mathbf{Y}_{k-1,i-1}) \\ &\quad + \Delta s[(\mathbf{M}_{k-1,i} + \mathbf{M}_{k-1,i-1})(\mathbf{Y}_{k-1,i} - \mathbf{Y}_{k-1,i-1}) + (\mathbf{M}_{k,i} + \mathbf{M}_{k,i-1})(\mathbf{Y}_{k,i} - \mathbf{Y}_{k,i-1})] \\ &\quad + \Delta t \Delta s(\mathbf{P}_{k-1,i-1} + \mathbf{P}_{k-1,i} + \mathbf{P}_{k,i-1} + \mathbf{P}_{k,i}) = 0, \end{aligned} \tag{28}$$

which represents a system of $n_e = 13$ equations and involves the dependent variables at two neighbouring points k and $k-1$. Upon writing equation (28) for all discrete points $(k-1/2, i-1/2)$, $k = 2, 3, \ldots, n_p$ and together with the boundary conditions at the end points $k = 1$ and $k = n_p$, we obtain a system of $n_e n_p$ equations for $n_e n_p$ unknowns, which can be solved efficiently by the relaxation method.

Note that the values of space and time discretizations, Δs and Δt are determined through convergence tests based on the required accuracy in the solution, but this is not an automated process. For the problems studied in section 4, Δs and Δt are chosen to be sufficiently small so that the deviation in the simulation results resulting from doubling the number of points used is $<1\%$.

4. NUMERICAL SOLUTIONS APPLIED TO SYSTEMS WITH SYNTHETIC LINES

We investigate numerically the dynamic behaviour of (a) a breaking synthetic line; and (b) a moored buoy subject to wave action. In both cases synthetic lines are subject to large deformations and loads, including cases of zero tension response. The applications serve to demonstrate the capability introduced by the formulation outlined in the previous sections; while the dynamic response of the individual systems is of great theoretical and practical interest.

4.1. POST-BREAKING BEHAVIOUR OF A SYNTHETIC LINE

Synthetic cables stretch up to thirty times more than steel cables before reaching their breaking strength. Thus they can store much larger potential energy for the same external load, than wire ropes. This energy is rapidly transformed into kinetic energy when the cable breaks. Observations of breaking towlines confirm that the cables snaps back at high velocity and can be extremely destructive. Serious damage to equipment and, more importantly, injuries to personnel have been reported by the U.S. Navy.

So far, only experimental methods have been used to study the dynamics of a tensioned synthetic line after failure, because of the difficulties involved in simulating large motions at very high speeds and rapidly varying tension. Feyrer [16] conducted a series of experiments to study the behaviour of synthetic ropes made of various materials and construction types after they broke. Bitting [17] conducted a similar series of experiments involving smaller ropes. Due to the high speed of the phenomenon of line breaking, experimental results are used primarily for qualitative understanding of the mechanisms involved; their high cost does not allow a systematic investigation of the effect of the principal parameters.

4.1.1. *Problem definition*

Consider a 60 m long synthetic cable whose end-points are held fixed at the same vertical level. The catenary shape of the cable will lie in the vertical plane containing its two end-points. In our study, we choose a cable with cross-sectional area $1{\cdot}964 \times 10^{-3}$ m^2 and density $\rho = 1140$ kg/m^3.

The tension–strain relation of the cable is the functional expression $T = p_1 \tanh(p_2\varepsilon + p_3) + p_4 + p_5\varepsilon$ which is obtained by fitting the data provided by Bitting [12]. The coefficients of the tension–strain relation are: $p_1 = 2{\cdot}703 \times 10^5$ N, $p_2 = 10{\cdot}2$, $p_3 = -2{\cdot}128$, $p_4 = 2{\cdot}627 \times 10^5$ N, and $p_5 = 135{\cdot}5$ N.

The cable is held at its initial position by horizontal and vertical forces applied at the end-points, and we assume that at time $t = 0$ the cable breaks at one of the end-points. In order to simulate the cable breaking, the horizontal and vertical external forces acting at one end are quickly but smoothly reduced to zero. The horizontal force, F_h, and the vertical force, F_v, both reach zero at $t = t_{br}$, called the *fracture time*, which turns out to be a critical parameter of the problem. This is physically equivalent to the fracture time in experiments where a cut is made near a cable end, under high load: after fracture initiates, the cable breaks progressively as more and more fibers adjacent to the cut fail, because they carry a substantially larger load, until the cable is severed. The force variation with time is modeled as:

$$F_h = F_{h,s} \cos^2\left(\frac{\pi}{2}\frac{t}{t_{br}}\right), \qquad F_v = F_{v,s} \cos^2\left(\frac{\pi}{2}\frac{t}{t_{br}}\right),$$

where $F_{h,s}$ and $F_{v,s}$ are the static horizontal and vertical forces at the end of the cable, respectively.

4.1.2. *Fast breaking cables*

To assess the effect of the initial static tension on the dynamic behaviour of the breaking line, we perform four simulations with different initial static tensions. For the case of low tension (hereinafter denoted case 1), the initial static tension is chosen to be 45 000 N which produces a static strain of 9·9%. For intermediate tension, we consider two cases with the static tensions of 180 000 N producing a strain of 17·8% (case 2) and 315 000 N producing a strain of 22·8% (case 3). For the high-tension case (case 4), we impose the static tension of 450 000 N which causes a strain of 29·2%. For all simulations, the breaking time is chosen to be $t_{br} = 5$ ms. Note that the imposed tension in case 4 is the quasi-static breaking tension for the cable under consideration. Thus, in case 1 the cable is broken at a static tension which is 10% of its breaking strength, while in cases 2 and 3 the cable is broken at tensions that correspond to 40 and 70% respectively of the cable's breaking strength.

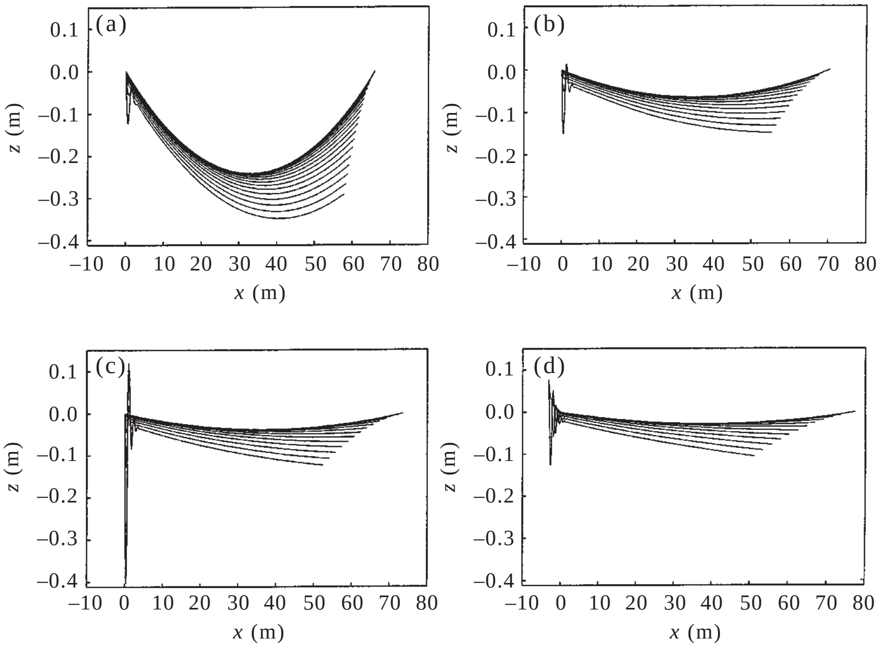

Figure 2. Motion of a breaking line (breaking time: 5 ms): (a) case 1 ($F_{h,s}$ = 45 000 N); (b) case 2 (180 000 N); (c) case 3 (315 000 N); (d) case 4 (450 000 N).

Figure 2 shows the x–z motion of the breaking cable, with the successive configurations of the line plotted at 10 ms apart. The total time, t_T, covered by the successive plots is different for each case: $t_T = 0{\cdot}20$ s, 0·14 s, 0·13 s, and 0·12 s for cases 1, 2, 3, and 4, respectively. A longitudinal wave travels along the cable at the elastic wave speed. The wave speed can be accurately estimated using the value of the static tension; the wave takes $t_* = 0{\cdot}55$–$0{\cdot}91$ s to travel along the whole length of the cable. Thus, the breaking time and time intervals covered by the simulations are appropriate.

From Figure 2, we see that lines breaking at higher tension experience a larger snap-back. Also the vertical motion of the breaking line decreases as the static tension increases. Finally, we note that the cable is "buckling" at the left end, which is the fixed end. In the high-tension case, the momentum of the recoiling part of the line is so large that it causes parts of the cable to overshoot and move to the left of the fixed point.

Figure 3 shows the variation of the tension along the cable, as function of time. The horizontal axis is the unstretched Lagrangian coordinate (s) while the vertical axis is the tension in N. Notice that the plots for cases 1 and 2 have different tension scales than plots for cases 3 and 4. The total time shown and the time elapsed between successive lines are the same as in the $x - z$ motion plots (cf. Figure 2).

The almost horizontal line at the top of each plot in Figure 3 marks the initial *static* tension for this case. The lines following this initial line show the tension dropping to zero at the right end, and the front of the unsteady tension propagating towards the fixed end. For the discussion on the behaviours of the propagation speed of the front, we define T' by

$$T'(\varepsilon) = \mathrm{d}T/\mathrm{d}\varepsilon, \tag{29}$$

hence for a linearly elastic material $T' = EA$ where E denotes the Young's modulus of the material and A the cross-sectional area. For a synthetic cable the stress–strain relation is non-linear, hence necessitating the use of T' in the problem formulation rather than the linear elastic stiffness EA.

The speed of propagation of the front, identical to the speed of propagation of elastic waves [25], is given by $c_e = [T'(\varepsilon)/m]^{1/2}$. Clearly the front speed depends on the initial static tension and thus it is different for each case. For high-tension cases, the speed reaches about 500 m/s, which is supersonic relative to the surrounding air. Such a supersonic wave can cause an acoustic wave drag on the cable, which, however, is expected to be small due to the very small lateral motion of the cable [26].

Notice that due to the presence of an inflection point in the tension–strain relation, the tension fronts in cases 2 and 3 propagate along the cable at faster speeds than that in case 4. Hence, for cases 2 and 3, we can see a shock beginning to form. At these high tensions the stress–strain relation is concave down and we retrieve the *shock forming during unloading* described in Courant and Friedrichs [27]. Here the shock does not form completely because the wave reaches the fixed end. Shock waves have been studied by Tjavaras and Triantafyllou [28] for synthetic cables subject to a sudden end load or imposed motion.

Finally, in Figure 4 the variation with time of the velocity of each point of the cable is plotted. As for the tension plots, the horizontal axis is the unstretched Lagrangian coordinate in m. The vertical axis is the velocity of the cable elements in m/s. The total time plotted and the time elapsed between each line are the same as in Figures 2 and 3.

In each plot of Figure 4, a horizontal line shows the initial velocity which is zero. The velocity increases at the right end where the breaking occurs, and the front of non-zero velocity propagates towards the fixed end. This front propagates at the same speed as the "non-zero static tension" front described above. Another front, the one at the highest

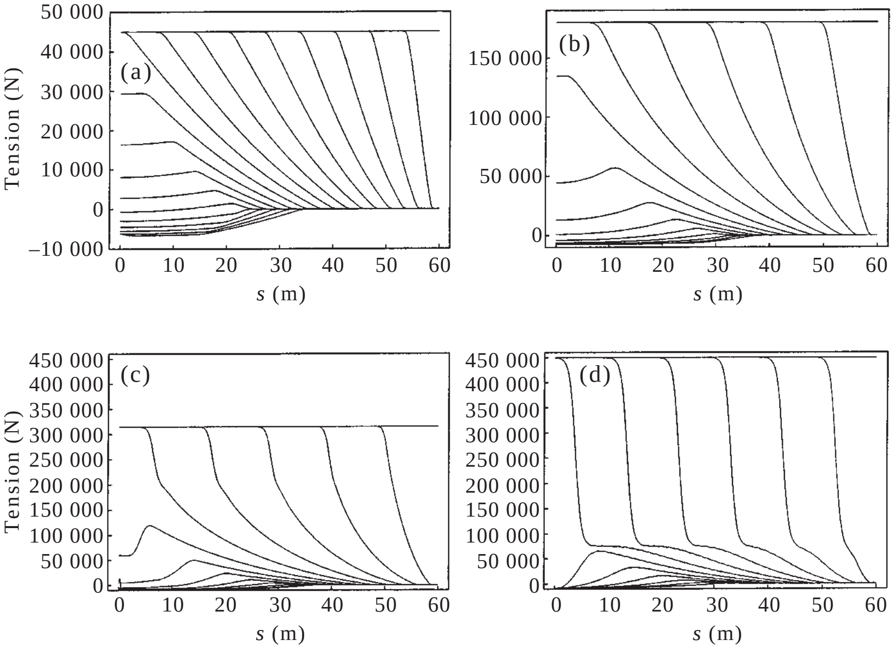

Figure 3. Time variation of the tension distribution of a breaking line (breaking time: 5 ms): key as in Figure 2.

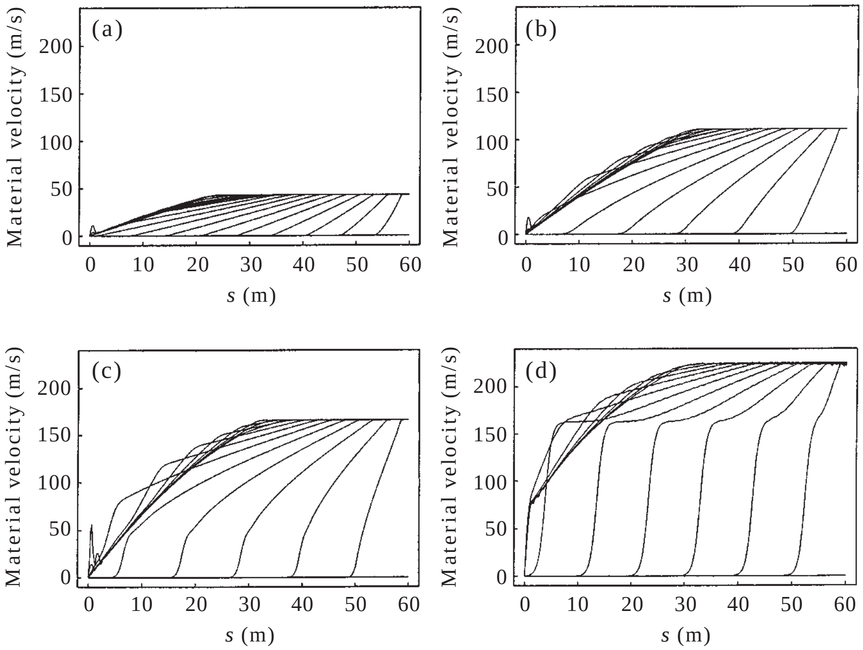

Figure 4. Time variation of the velocity distribution of a breaking line (breaking time: 5 ms): key as in Figure 2.

velocity for each run, also propagates along the cable. This front propagates at the same speed for all cases, because this is the speed of propagation of elastic waves at zero tension ($[T'(0)/m]^{1/2}$). The segment of the cable to the right of this front is under zero tension and is being pulled towards the fixed end by the rest of the line.

Figure 4 also indicates that the velocity of the end-point, which is the maximum spanwise velocity in every case, is higher when the initial static tension is higher. This finding is an expression of the fact that more energy is stored in the lines that are more highly tensioned. Notice that for the high-static-tension case, the velocity of the broken end reaches values comparable to the speed of sound in air.

4.1.3. *Slowly breaking cables*

It has been postulated that cables that break slowly are safer. By "slowly-breaking" we mean that the value of the tension at the breaking point takes longer to reach zero. Cables have been designed so that their strands do not fail all at the same time but sequentially, to prevent a sudden rupture. Thus, the intact strands continue to carry loads which are smaller than the static tension on the line but larger than zero, and the rest of the force is taken up by inertia forces. In order to assess the effect of the time it takes for the tension to drop from its static value to zero, we perform another four simulations (cases 1′–4′) with the breaking time extended to $t_{br} = 50$ ms while the static tensions are kept the same as for cases 1–4.

Figure 5 shows the post-fracture motion of the breaking line in the x–z plane at 10 ms intervals. Comparing these results with those in Figure 2, we observe that the overall motion of the centreline is not significantly affected by the slower breaking time. Like the fast-breaking case, the configuration with higher static tension obtains a larger snap-back but a less pronounced vertical motion. Again, buckling of the cable occurs for all static tensions in the region close to the cable's fixed end.

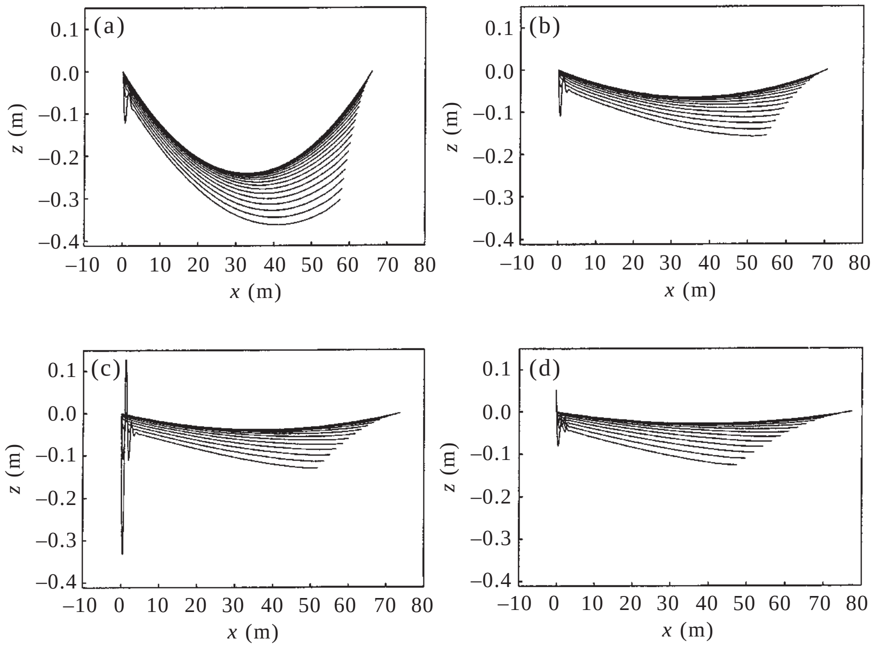

Figure 5. Motion of a breaking line (breaking time: 50 ms): (a) case 1′ ($F_{h,s} = 45\,000$ N); (b) case 2′ (180 000 N); (c) case 3′ (315 000 N); (d) case 4′ (450 000 N).

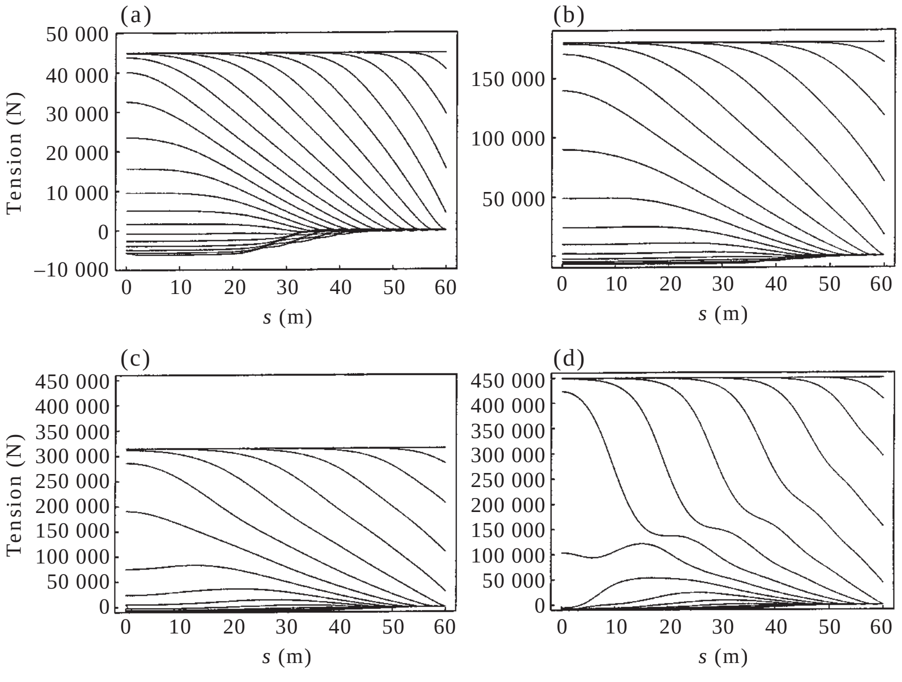

Figure 6. Time variation of the tension distribution of a breaking line (breaking time: 50 ms): key as in Figure 5.

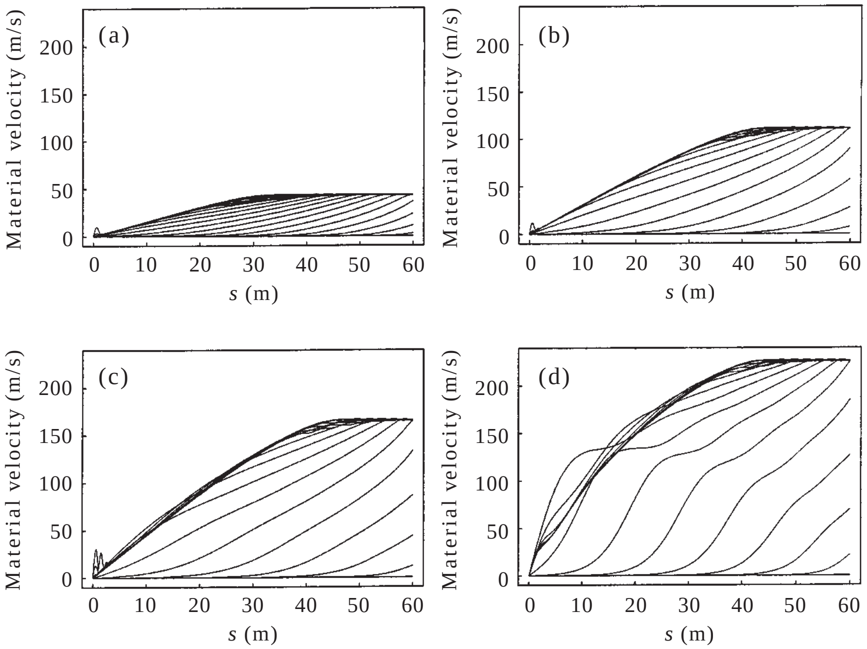

Figure 7. Time variation of the velocity distribution of a breaking line (breaking time: 50 ms): key as in Figure 5.

The similarity in the x–z motion between the fast-breaking and slowly-breaking cases hides, however, significantly differences that can be seen in the tension plots and the cable–velocity plots. Figure 6 shows the time variation of the tension distribution along the cable, where the scales as well as the time elapsed between successive lines are identical to those in Figure 3. Clearly, when the breaking time is larger, the tension is seen to be more uniformly distributed along the cable. Indeed it takes longer time for the tension at the breaking end to reach zero and the non-zero-tension wave has time to propagate to the fixed end, thus making the variation in the tension less sharp. This has a noticeable effect on the velocity distribution.

Figure 7 shows the time variation of the cable velocity spanwise distribution. By comparing to the fast breaking case (cf. Figure 4), we find that the maximum velocity in the cable is not affected by the fracture time; the initial static tension is the dominant parameter affecting the maximum velocity. On the other hand, the time until the maximum velocity is reached varies: in the slowly breaking cases it takes longer for the maximum velocity to be reached at the breaking end. Also, the portion of the length of cable that moves at this maximum velocity is smaller in the slowly breaking runs, indicating that the kinetic energy is more uniformly distributed in the line. Hence, even though the total kinetic energy that must be dissipated after breaking depends only on the static tension and does not depend on the breaking time, the way the energy is dissipated does. Lines that are breaking more slowly dissipate the energy along a larger part of their length. Fast breaking cables have a portion of their length moving at maximum velocity and another part practically motionless, whereas slowly breaking cables have a larger part moving at moderate velocities and only a small region near the broken end moves at maximum speed. This is a possible explanation for the generally accepted view that slowly breaking lines are somewhat less destructive than fast breaking ones.

4.2. DYNAMIC BEHAVIOUR OF MOORED BUOYS EXCITED BY FREE SURFACE WAVES

We study the problem of dynamic response of a buoy tethered with a relatively short tether in finite water depth, under the influence of incident water waves, as shown in Figure 8. Large buoy motions may be excited when a synthetic rope is used due to the large extensibility of the material. We consider the qualitative dynamic properties of the system through long numerical simulation of the response.

We consider the buoy to be a sphere with diameter D. The upper end of the cable is considered to be attached at the centre of the spherical buoy, while the lower end is fixed at the bottom. The average depth of the water is H. We consider long waves compared to the diameter of the buoy; hence the hydrodynamic loads on the buoy and the cable can be approximated by Morison's equation. The equation of motion for the buoy is

$$(M + M_a)\frac{\mathrm{d}U}{\mathrm{d}t} = (\rho_w V + M_a)\frac{\mathrm{d}\mathbf{U}_w}{\mathrm{d}t} + \mathbf{B} - \mathbf{W} - \mathbf{T} - \tfrac{1}{2}\rho_w C_d A_p(\mathbf{U} - \mathbf{U}_w)|\mathbf{U} - \mathbf{U}_w|, \quad (30)$$

where M is the mass of the buoy, M_a its added mass, and V its volume. Here the vector $\mathbf{U}$ denotes the velocity of the buoy, $\mathbf{U}_w$ the flow velocity due to the incoming waves, $\mathbf{T}$ the tension at the upper end of the cable, and $\mathbf{B}$ the buoyancy and $\mathbf{W}$ the weight of the buoy. In addition, C_d is the viscous drag coefficient and A_p the projected area of the buoy. Since the buoy is spherical, the added mass, M_a, and the projected area, A_p, are the same in all

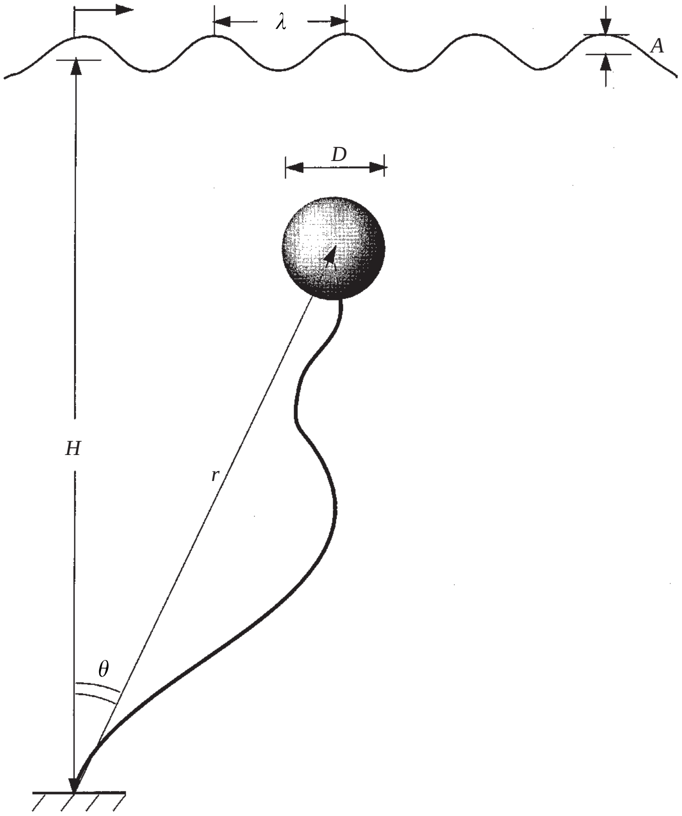

Figure 8. A buoy tethered in surface waves.

TABLE 1

Physical characteristics of tether–sphere system for the simulations

Tether	
Unstretched length	$l_0 = 20$ m
Cross-sectional area	$= 7{\cdot}85 \times 10^{-5}$ m^2
Density	$\rho = 1140$ kg/m^3
Sphere	
Diameter	$D = 1{\cdot}5$ m
Mass	$M = 1611$ kg
Added mass	$M_a = 907$ kg
Drag coefficient	$C_d = 0{\cdot}2$

directions. The three components of the vector equation (30), in the tangential, normal and binormal directions, provide the boundary conditions at the upper end of the cable.

We consider uni-directional incident waves; hence the motions of the cable and the buoy are planar. An unstable out-of-plane response can be excited under conditions of cable snapping described later. A polar coordinate system (r, θ) is chosen to represent the position of the buoy, where r is the distance from the lower end of the cable to the centre of the buoy and θ the angle from the vertical direction. The physical characteristics of the cable and sphere used in our simulations are given in Table 1. For this problem, we choose a linear strain–tension relation $T = p_1\varepsilon$ and $p_1 = 5 \times 10^4$ N.

We use the static solution as the initial condition for the dynamic simulation. When at rest, the cable is elongated to a length $l_0 + \Delta l$, with $\Delta l \simeq 0{\cdot}04 l_0$, because of the buoyancy; and the buoy lies at the position $(l_0 + \Delta l, 0)$. The static tension at the upper end of the cable is $\mathbf{T}_s = \mathbf{B} - \mathbf{W}$.

An incident wave with period $T_i = 5$ s, typical of water waves, is imposed on the free surface. The cable–buoy system is excited by the hydrodynamic loads and begins to oscillate about its equilibrium position. We find that the character of the response may be drastically different depending on the amplitude of the incident waves. For small incident-wave amplitudes, the cable remains tensioned at all times and the motion of the buoy is periodic and regular. However, when the amplitude of the incident wave is larger than a threshold value, the tension exhibits alternately an interval of near-zero value, followed by a period of rapid tension built-up; then, the motion of the buoy is found to be chaotic. To illustrate these properties, numerical results obtained for two different incident wave steepnesses, viz. $kA = 0{\cdot}016$ and $kA = 0{\cdot}13$, are presented in the following two sections.

4.2.1. *Small incident wave amplitude*

First, we consider the case with the incident wave amplitude $A = 0{\cdot}1$ m and the associated wave slope $kA = 0{\cdot}016$. The hydrodynamic forcing due to the incident waves is periodic so the buoy oscillates about its equilibrium position (r_0, θ_0) $(r_0 = l_0 + \Delta l$ and $\theta_0 = 0)$. Correspondingly, the length of the cable varies periodically around its mean value $l_0 + \Delta l$. Because the wave forcing is small, the amplitude of the motion Δr is less than the static value Δl. As a result, the cable retains a positive value of tension at all times and the cable–buoy system responds similar to a driven second-order (mass–dashpot–spring) system.

In the numerical simulations, the motion of the buoy starts impulsively from rest; hence, in addition to the forced response the numerical results contain a transient response, consisting of the natural modes of the system, which decays with time. The natural frequencies and modes can be easily estimated from the equation of motion of the buoy. Upon neglecting the coupling effect, the natural frequencies in the r- and θ-directions are obtained to be given by $\omega_{nr} = [p_1/l_0(M + M_a)]^{1/2}$ and $\omega_{n\theta} = [T_s/l_0(M + M_a)]^{1/2}$, respectively. In the present case, it is found that $\omega_{nr} \approx 1{\cdot}0$ rad/s and $\omega_{n\theta} \approx 0{\cdot}2$ rad/s. The forcing frequency is the wave frequency, $\omega_i = 2\pi/T_i = 1{\cdot}26$ rad/s.

Figure 9 shows the time history of the cable tension at the connection with the buoy. As expected, the transient response decays slowly due to the presence of viscous (quadratic) damping. For the present case, with small incident wave amplitude, the cable retains a positive tension at all times. Also, there are no internal resonances, and coupling between the two motions is nearly negligible.

As shown in Figure 10, the motion of the buoy in the radial direction consists of forced and transient terms, exhibiting similar trends as the cable tension. Analogous results are also obtained for the motion of the buoy in the angular direction, as shown in Figure 11, except that the transient response vanishes more slowly owing to its much lower natural frequency.

Figure 12 shows the spectra of the two components of buoy motion. The spectral amplitude of the radial motion at frequency ω is obtained as

$$\Delta\tilde{r}(\omega) = \frac{1}{nT_i}\int_{\tau_0}^{\tau_0 + nT_i} \Delta r(t)\, \mathrm{e}^{i\omega t}\, \mathrm{d}t, \tag{31}$$

with a similar expression for the angular component $\Delta\tilde{\theta}$. For results in Figure 12, the integer n is chosen to be 20 and $\tau_0 = 40T_i$. For both radial and angular motions, the natural and wave-forcing modes are seen to dominate the response. And the numerical values of the natural frequencies agree quite well with the estimated values.

4.2.2. *Large incident wave amplitude*

Next we increase the incident wave steepness to $kA = 0{\cdot}13$, causing a correspondingly larger buoy response. Due to the large buoy motions, the cable is at times under effective compression, when the radial buoy motion is towards the anchor direction. The bending stiffness is small, hence the cable buckles, assuming a high order buckling mode. As the buoy motion reverses direction moving away from the anchor, tension builds rapidly in the cable reaching high, impulse-like peaks, which eventually arrest the motion of the buoy, and reverse its direction. The phenomenon of nearly-impulsive tension built up and loss is called *cable snapping*. Figure 13 shows the tension as function of time in a snapping cable: large tension peaks are followed by intervals of near-zero tension.

Because of the similarity of the snapping cable–buoy system behaviour to that of a system with a piece-wise linear restoring force [29, 30] or the bouncing-ball problem [31], which have been shown to exhibit chaotic behaviour under certain excitation conditions, we investigated the dynamic properties of the cable–buoy system. An essential characteristic of chaotic response is extreme sensibility to small variations in initial conditions. For a chaotic motion, two trajectories with slightly different initial conditions diverge exponentially from each other. This feature is often quantified through the Lyapunov exponents. Beginning with two trajectories, a reference trajectory and a nearby trajectory, and if the motion is chaotic, the two trajectories diverge from each other exponentially; hence we have

$$d \propto 2^{\sigma t/T_i}, \tag{32}$$

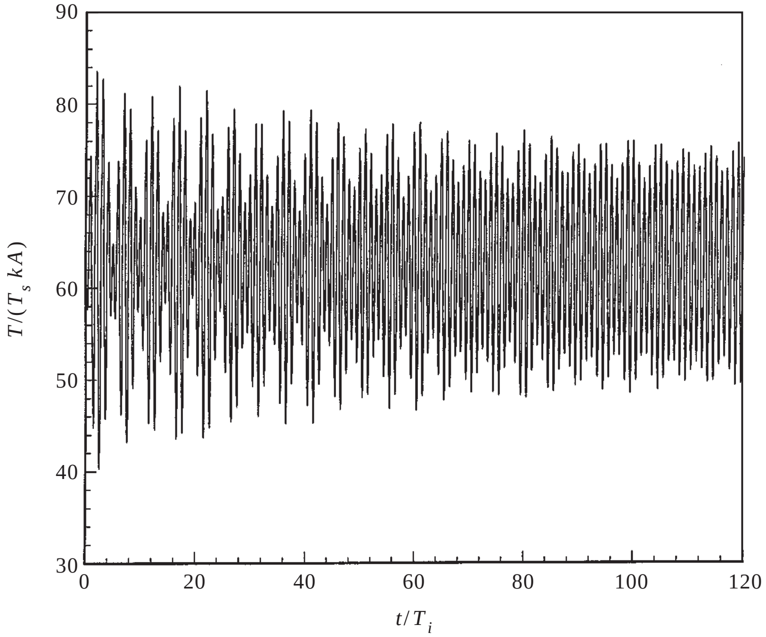

Figure 9. The tension of the cable at the top end ($T_i = 5$ s and $kA = 0{\cdot}016$).

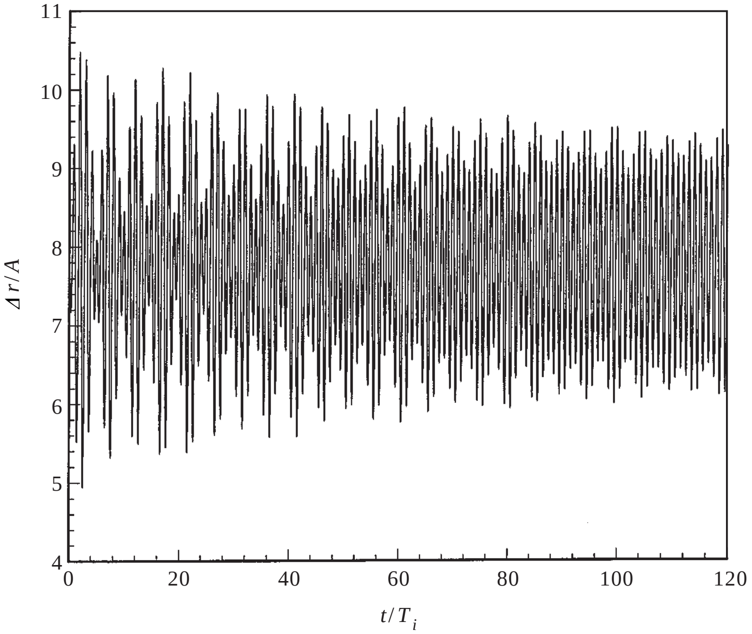

Figure 10. The motion of the buoy in the radial direction ($T_i = 5$ s and $kA = 0{\cdot}016$).

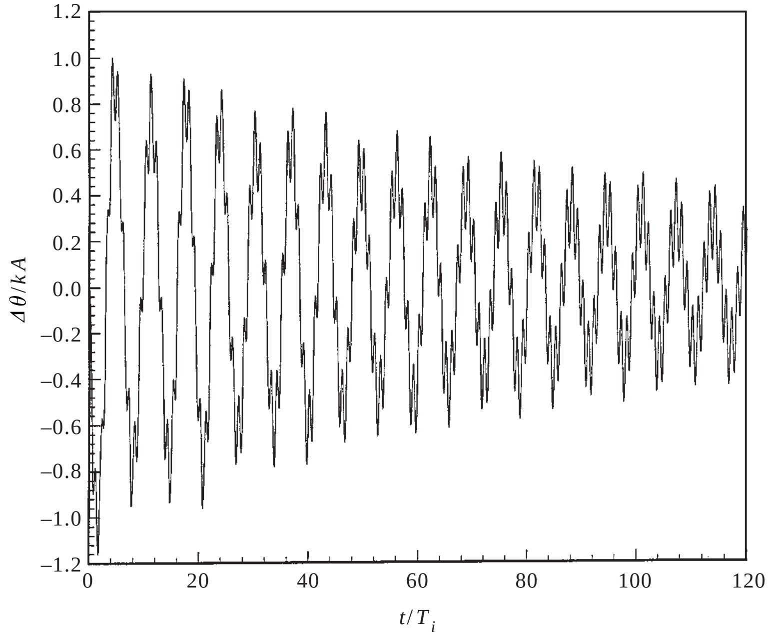

Figure 11. The motion of the buoy in the angular direction ($T_i = 5$ s and $kA = 0{\cdot}016$).

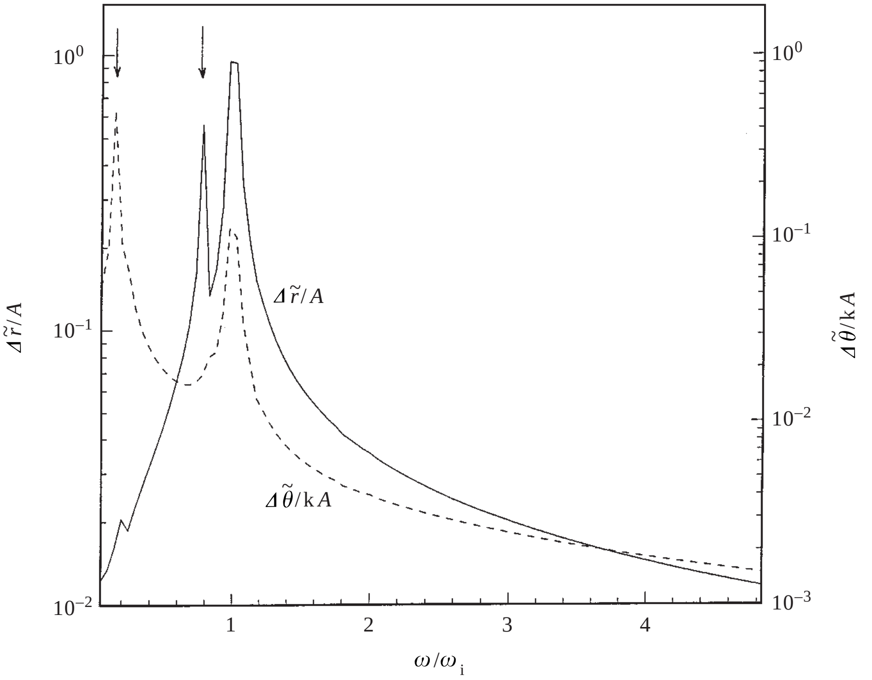

Figure 12. The spectra of the buoy motion. The results plotted are: ——, in the radial direction; –––, in the angular direction. Theoretical prediction of the natural frequencies of the buoy system in waves is indicated by ↓ ($T_i = 5$ s and $kA = 0{\cdot}016$).

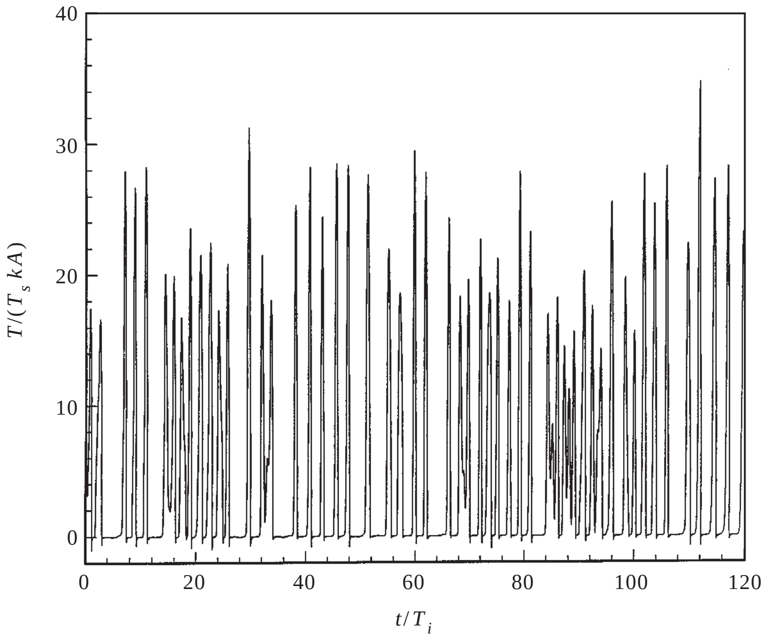

Figure 13. The tension of the cable at the top end ($T_i = 5$ s and $kA = 0{\cdot}13$).

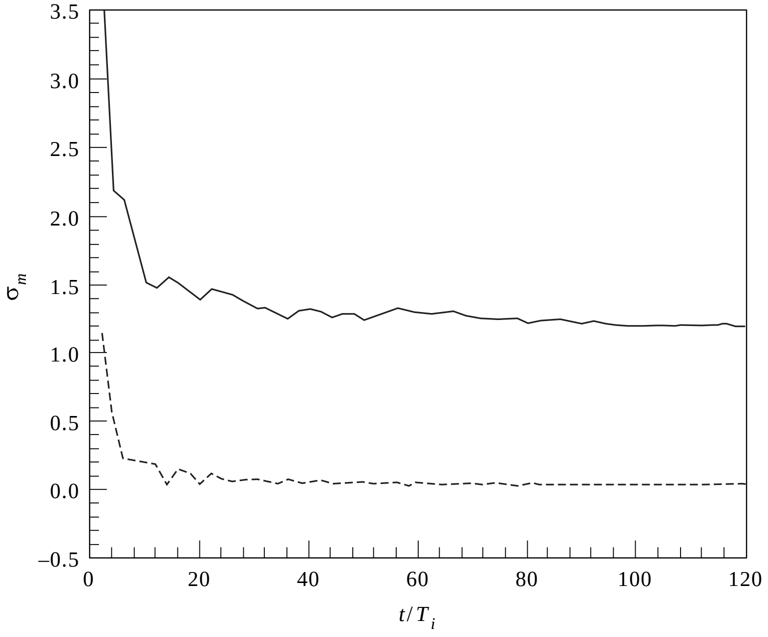

Figure 14. The time variation of the maximum Lyapunov exponent σ_m for the buoy motion in the radial direction. The results plotted are: ——, for the case of the incident wave steepness $kA = 0{\cdot}13$; ---, for the case of $kA = 0{\cdot}016$ ($T_i = 5$ s).

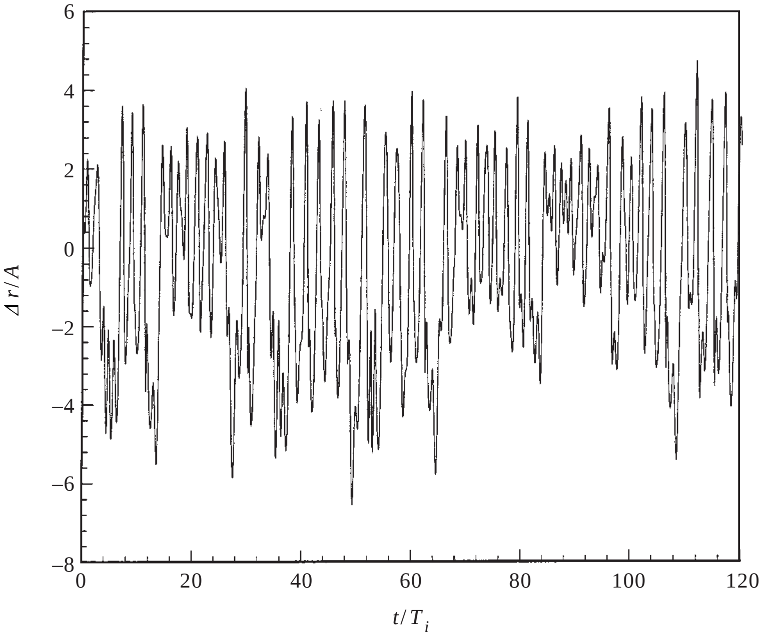

Figure 15. The motion of the buoy in the radial direction ($T_i = 5$ s and $kA = 0{\cdot}13$).

where d represents the distance between the two trajectories, and the dimensionless parameter σ is the Lyapunov exponent. A positive value of the Lyapunov exponent is an indication of chaos. To obtain the maximum Lyapunov exponent σ_m in the present case, we apply the method of Wolf *et al*. [32] which involves the reconstruction of pseudo-phase

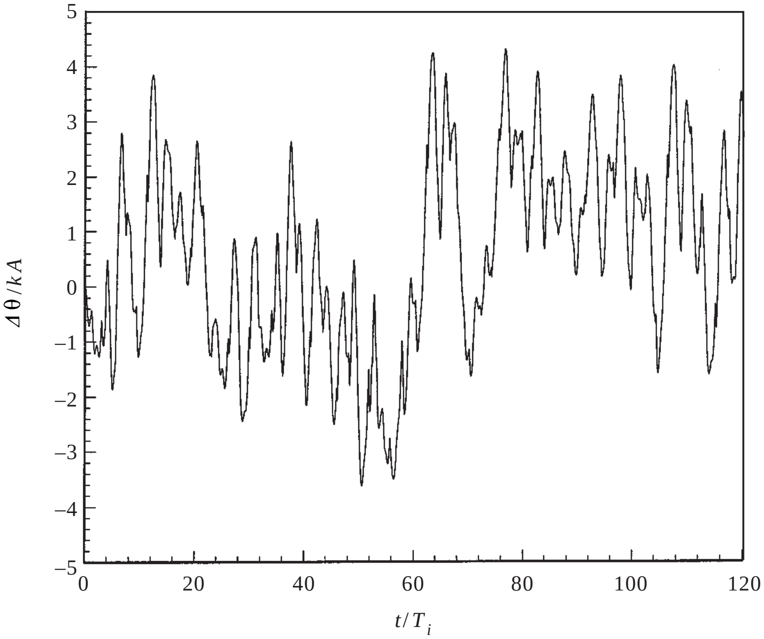

Figure 16. The motion of the buoy in the angular direction ($T_i = 5$ s and $kA = 0{\cdot}13$).

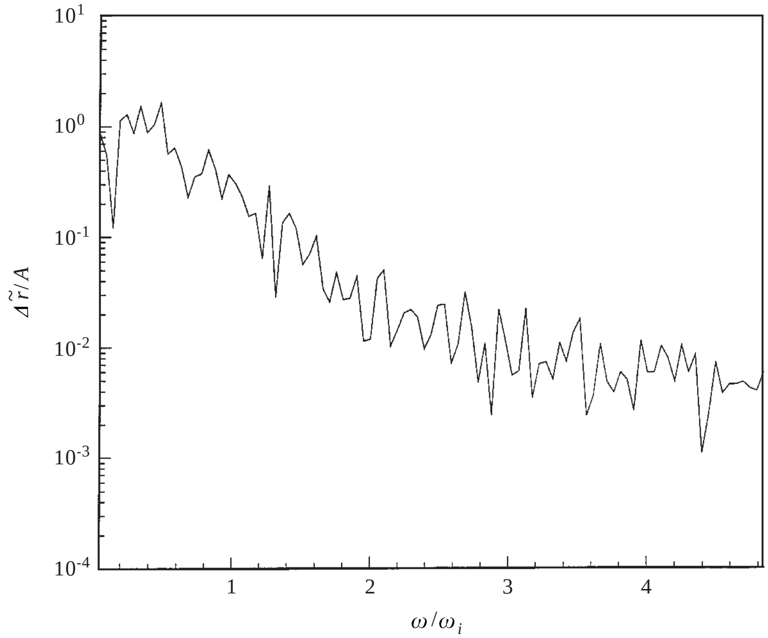

Figure 17. The spectrum of the buoy motion in the radial direction ($T_i = 5$ s and $kA = 0{\cdot}13$).

space from time–history data. Figure 14 shows the values of the Lyapunov exponent as function of time. For the small incident wave case ($kA = 0{\cdot}016$), the Lyapunov exponent is seen to approach zero as time increases, implying regular motion. For the larger incident

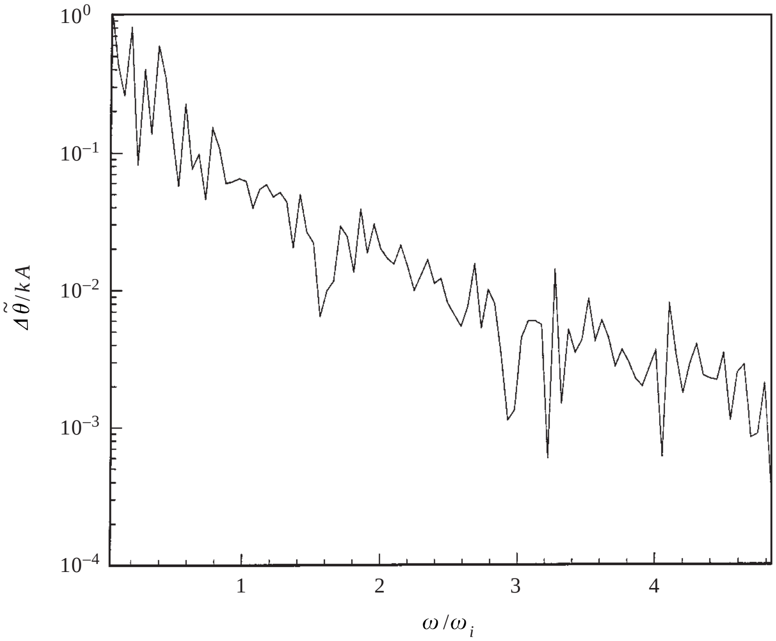

Figure 18. The spectrum of the buoy motion in the angular direction ($T_i = 5$ s and $kA = 0{\cdot}13$).

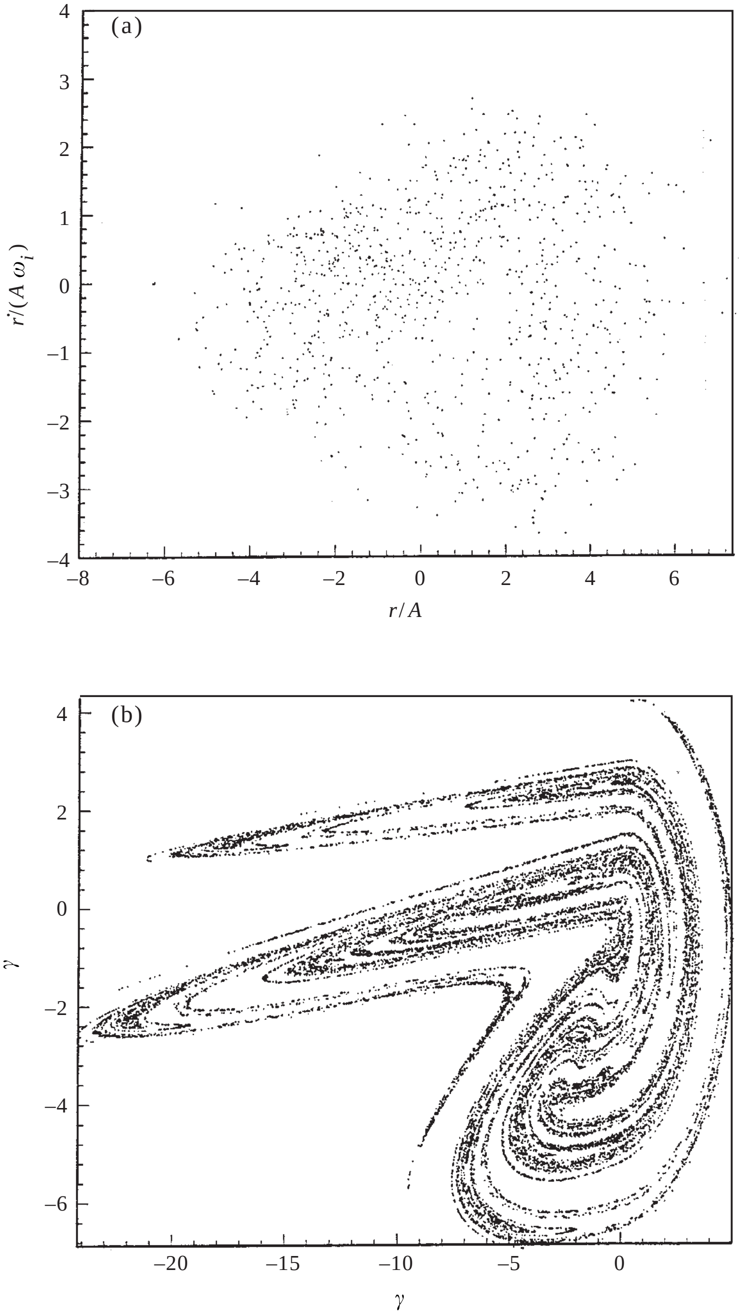

Figure 19. Poincaré sections of the buoy motion obtained (a) from the exact model; and (b) from the approximate model with parameters in equation (33) given by $F = 1{\cdot}4$, $B - W = 0{\cdot}68$, $\mu = 0{\cdot}025$, and $\omega = 1{\cdot}14$.

wave case ($kA = 0{\cdot}13$), however, a positive Lyapunov exponent is obtained, indicating chaotic motion.

The time histories of the motions of the buoy in the radial and angular directions are displayed in Figures 15 and 16, respectively. Unlike the small wave case ($kA = 0{\cdot}016$), where the responses of the buoy are periodic and regular (cf. Figures 10 and 11), both the radial and angular buoy motions are non-periodic and appear to be irregular. This becomes more apparent in the plots of spectra of the motions, shown in Figures 17 and 18 respectively for the radial and angular motions. Unlike the small wave case where the natural and forcing modes are dominant (cf. Figure 12), the spectra of the motions are continuous for a wide range of frequencies and no apparent dominant modes are shown.

The global behaviour of the dynamic buoy–cable system can be understood in terms of characteristics of the Poincaré surface of section in the phase space. Figure 19(a) shows the Poincaré map which is the plot of the displacement versus the velocity of the buoy in the radial direction. Clearly, the points in Figure 19(a) fall in a region and hence the buoy motion is chaotic. Since the complete Poincaré section represents a four-dimensional surface for the present two-degrees-of-freedom dynamic system, its projection onto a plane in two variables in Figure 19(a) does not show a clear fractal structure of the Poincaré map.

To obtain the Poincaré map showing fractal structure characteristic of a strange attractor, we consider the buoy motion in the radial direction by neglecting the coupling effect with the motion in the angular direction. The equation of motion of the buoy is much simplified and can be expressed in the form

$$\ddot{\gamma} + \mu\dot{\gamma} + a\gamma = F \sin \omega t + B - W, \qquad (33)$$

where all quantities are normalized in terms of the mass of the buoy, the diameter of the buoy, and the natural frequency of the radial motion. Here γ denotes the radial motion, $a = 1$ for $\gamma \geqslant 0$ and $a = 0$ for $\gamma < 0$ represents the restoring effect associated with cable snapping, F is the amplitude of wave excitation, and B the buoyancy and W the weight of the buoy. Also a linear damping term $\mu\dot{\gamma}$ is included to account for surface wave radiation due to the buoy oscillation. The plot of the *Poincaré* section from equation (33) is shown in Figure 19(b) where the fractal structure of a strange attractor is evidently seen.

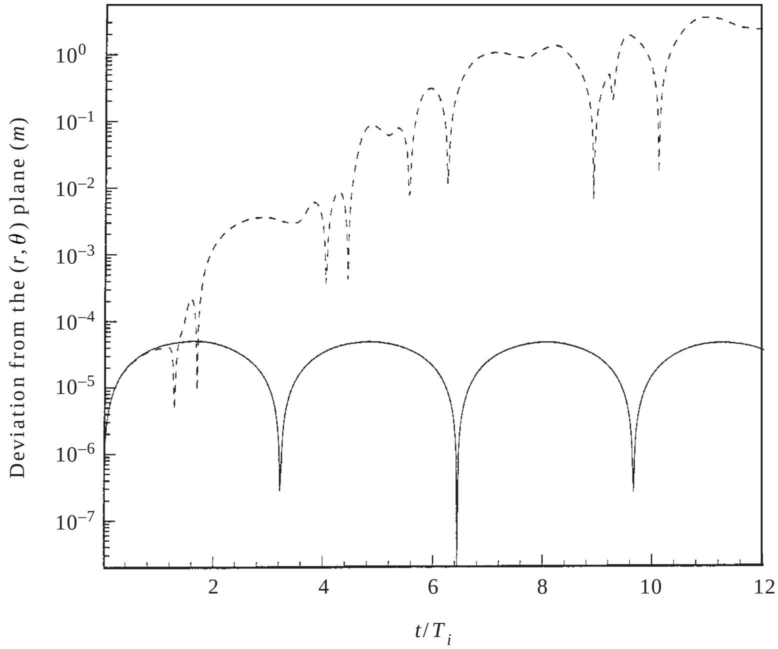

Figure 20. The stability of the planar motion of the cable–buoy system to the out-of-plane disturbance. The results plotted are the time variations of the buoy motion in the direction normal to the centre plane of the buoy–cable system with the incident wave steepness $kA = 0{\cdot}016$ (——) and $kA = 0{\cdot}13$ (- - -) ($T_i = 5$ s).

Note that the motions of the buoy and cable are planar under the action of surface-wave loads which are symmetric about the plane of the static cable–buoy system. However, the planar motion of the cable may not be stable to an out-of-plane disturbance, particularly at low tension [33]. For hanging chains under harmonic excitations, Howell and Triantafyllou [34] found that both two- and three-dimensional responses can be excited by planar forcings.

To examine the stability of the planar motion of the cable–buoy system under surface waves, we numerically study the growth of an out-of-plane disturbance which is artificially added to the dynamic system. In simulations, the initial disturbance applied is a small velocity of the buoy (10^{-5} m/s) which is perpendicular to the wave loads on the cable and buoy. Figure 20 shows the time evolution of the out-of-plane motion of the buoy for two incident wave steepnesses: $kA = 0{\cdot}016$ and $0{\cdot}13$. For the small incident wave case ($kA = 0{\cdot}016$), it is observed that the out-of-plane motion does not grow with time and thus the motions of the cable and buoy are two-dimensional and stable. For the large incident wave case ($kA = 0{\cdot}13$), however, the out-of-plane motion is seen to grow exponentially and reach the value comparable to the in-plane motion (in magnitude). As a result, the total response of the system becomes three-dimensional, which is similar to the problem of hanging chains [34].

5. CONCLUSIONS

We developed a set of equations describing the motion of a highly-extensible cable, using Euler parameters to represent the relative rotation of the reference frames to avoid the singularity accompanying the Euler–angle representation. The bending stiffness of the cable is included to ensure a well-posed problem when the tension becomes small [15]. Finally an arbitrary tension–strain relation is allowed.

The equations are solved using finite differences and an implicit numerical integration scheme, which allows long-term simulation with error within pre-defined limits. To demonstrate the new method, we studied two problems: (a) the post-breaking behaviour of a synthetic cable, and (b) the dynamic response of a moored near-surface buoy in surface waves.

For the problem of a breaking cable we investigated the time evolution of the cable configuration, the tension distribution, and the velocity along the cable span after it breaks. The fracture time, i.e. the time between the onset and the completion of fracture, is a principal parameter; hence a fast-breaking case and a slow-breaking were studied in detail. We find that in the slow-breaking case, the tension-distribution along the cable is more uniform; on the other hand the maximum velocity in the cable is only affected by the tension inside the cable before breaking and is independent of the fracture time. The slowly-breaking cable dissipates the kinetic energy along a larger part of their length, thus explaining the generally-accepted view that such lines are less destructive.

The problem of the motion of an underwater buoy tethered by cable to the bottom requires long-term simulation of cable dynamics, which is possible under the present formulation, using Euler parameters and implicit time integration schemes. The cable–buoy system is excited to oscillate by the hydrodynamic loads induced by free-surface incident waves. When the incident wave amplitude is small, the cable tension remains positive and the motion of the buoy is regular, composed of natural (transient) modes and forced response. However, if the amplitude of the incident wave is larger than a threshold value, the tension becomes zero for part of the cycle, followed by large peaks resulting in a snapping response. The motions of the buoy become chaotic, resulting in the formation of strong surface signatures, which we provide in a companion paper [35].

ACKNOWLEDGMENT

Financial support has been provided by the Office of Naval Research (Ocean Engineering Division), under contract N00014-95-1-0010, monitored by Dr T. F. Swean Jr.

REFERENCES

1. H. M. Irvine 1981 *Cable Structures*. Cambridge, MA: MIT Press.
2. M. S. Triantafyllou 1991 *The Shock and Vibration Digest* **23**(7), 3–8. Dynamics of cables, towing cables and mooring systems.
3. A. P. Dowling 1988 *Journal of Fluid Mechanics* **187**, 507–532. The dynamics of towed flexible cylinders, part I: Neutrally buoyant elements.
4. M. S. Triantafyllou and G. S. Triantafyllou 1991 *Journal of Sound and Vibration* **148**(2), 345-351. The paradox of the hanging string: an explanation using singular perturbations.
5. J. J. Burgess 1992 In *Proceedings of the 11th International Conference on Offshore Mechanics and Arctic Engineering (ASME)*, pp. 283–289. Equations of motion of a submerged cable with bending stiffness.
6. M. S. Triantafyllou and C. T. Howell 1992 *Journal of Engineering Mechanics (ASCE)* **118**(4), 355–368. Nonlinear impulsive motions of low tension cables.
7. M. S. Triantafyllou and C. T. Howell 1993 *Journal of Sound and Vibration* **162**(2), 263–280. Nonlinear unstable response of hanging chains.
8. K. R. Bitting 1980 In *12th Offshore Technology Conference*, pp. 509–516, Houston. Cyclic tests of new and aged nylon and polyester line.
9. J. H. V. Leeuwen 1981 In *13th Offshore Technology Conference*, pp. 453–463. Dynamic behavior of synthetic ropes.
10. J. F. Flory 1991 In *Proceedings of MTS Conference* **2**, 653–660. Cyclic load testing of high-performance tension members.
11. H. Shin, K. Yamakawa and S. Hara 1994 In *Proceedings of the 13th International Conference on Offshore Mechanics and Arctic Engineering*, Vol. I, Offshore Technology, 441–448. Laboratory tests on synthetic fiber ropes.
12. K. R. Bitting 1985 *U.S. Department of Transportation Report No. CG-D*-10-85, *U.S. Coast Guard*. Dynamic modeling of nylon and polyester double braid line.
13. I. M. Ward 1983 *Mechanical Properties of Solid Polymers*. New York: Wiley. 2nd edition.
14. M. S. Triantafyllou and D. K. P. Yue 1995 *Journal of Sound and Vibration* **186**(3), 355–368. Damping amplification in highly extensible hysteretic cables.
15. M. S. Triantafyllou and C. T. Howell 1994 *Journal of Sound and Vibration* **173**(4), 433–447. Dynamic response of cables under negative tension: an ill-posed problem.
16. K. Feyrer 1978 *Technical Report, Department of Rope Research, University of Stuttgart, Germany*. Break tests carried out on various ropes in order to determine the energy of lash-back at break.
17. K. R. Bitting 1982 *Technical Report CG-D*-29-82, *U.S. Coast Guard Research and Development Center, Avery Point, Groton, CT*. A snap back evaluation technique for synthetic line.
18. W. Paul 1980 In *Proceedings of the Winter Annual Meeting (ASME)*, Ocean Engineering Division. Energy absorption of ropes.
19. M. A. Grosenbaugh 1996 *Ocean Engineering* **23**, 7–25. Dynamics of oceanographic surface moorings.
20. K. Idris, J. W. Leonard and S. C. S. Yim 1997 *Ocean Engineering* **24**, 445–464. Coupled dynamics of tethered buoy systems.
21. L. D. Landau and E. M. Lifshitz 1959 *Theory of Elasticity*. London: Pergamon Press.
22. F. S. Hover 1997 *Ocean Engineering* **24**(8), 765–783. Simulation of stiff massless tethers.
23. T. R. Goodman and J. P. Breslin 1976 *Journal of Hydronautics* **10**, 113–120. Statics and dynamics of anchoring cables in waves.
24. B. Wendroff 1960 *Journal of the Society of Industrial and Applied Mathematics* **8**(3), 549–555. On centered difference equations for hyperbolic systems.
25. M. Behbahani-Nejad and N. C. Pekins 1996 *Journal of Sound and Vibration* **196**, 189. Freely propagating waves in elastic cables.
26. P. M. Morse 1948 *Vibration and Sound*. New York: McGraw Hill.
27. R. Courant and K. O. Friedrichs 1948 *Supersonic Flow and Shock Waves*. New York: Springer.

28. A. A. Tjavaras and M. S. Triantafyllou 1996 *Journal of Engineering Mechanics* (*ASCE*) **122**(4). Shock waves in curved synthetic cables.
29. S. W. Shaw and P. J. Holmes 1983 *Journal of Sound and Vibration* **90**(1), 129–155. A periodically forced piecewise linear oscillator.
30. S. W. Shaw 1985 *Journal of Applied Mechanics* **52**, 453–464. The dynamics of a harmonically excited system having rigid amplitude constrains.
31. P. J. Holmes 1982 *Journal of Sound and Vibration* **84**, 173–189. The dynamics of repeated impacts with a sinusoidally vibrating table.
32. A. Wolf, J. B. Swift, H. L. Swinney and J. A. Vastano 1995 *Physica* **116D**, 285–317. Determining Lyapunov exponents from a time series.
33. N. C. Perkins and C. D. Mote 1989 *Journal of Sound and Vibration* **128**(3), 397–410. Theoretical and experimental stability of two translating cable equilibria.
34. C. T. Howell and M. S. Triantafyllou 1993 *Proceedings of the Royal Society*, *London A* **440**, 345–364. Stable and unstable non-linear resonant response of hanging chains: theory and experiment.
35. Q. Zhu, A. A. Tjavaras, Y. Liu, M. S. Triantafyllou and D. K. P. Yue 1998 *Journal of Fluid Mechanics* (submitted). Dynamics and free-surface signature of moored near-surface buoys on waves.

APPENDIX A: FORMS OF M AND P

The matrix $\mathbf{M}$ is a 13×13 matrix which is then split in the 13×6 matrix $\mathbf{M}_1$, the column vectors $\mathbf{M}_2$, $\mathbf{M}_3$, $\mathbf{M}_4$ and $\mathbf{M}_5$ and the 13×3 null matrix $\mathbf{0}$. The matrix $\mathbf{M}$ takes the form

$$\mathbf{M} = [\mathbf{M}_1 \quad \mathbf{M}_2 \quad \mathbf{M}_3 \quad \mathbf{M}_4 \quad \mathbf{M}_5 \quad \mathbf{0}] \tag{34}$$

with

$$\mathbf{M}_1 = \begin{bmatrix} 0 & 0 & 0 & -\dfrac{m}{f'(\varepsilon)} & 0 & 0 \\ 0 & 0 & 0 & 0 & -(m+m_a) & 0 \\ 0 & 0 & 0 & 0 & 0 & -(m+m_a) \\ -1 & 0 & 0 & 0 & 0 & 0 \\ 0 & 0 & 0 & 0 & 0 & 0 \\ 0 & 0 & 0 & 0 & 0 & 0 \\ 0 & 0 & 0 & 0 & 0 & 0 \\ 0 & 0 & 0 & 0 & 0 & 0 \\ 0 & 0 & 0 & 0 & 0 & 0 \\ 0 & 0 & 0 & 0 & 0 & 0 \\ 0 & 0 & 0 & 0 & 0 & 0 \\ 0 & 0 & 0 & 0 & 0 & 0 \\ 0 & 0 & 0 & 0 & 0 & 0 \end{bmatrix}, \tag{35}$$

$$\mathbf{M}_2 = \begin{bmatrix} -2m(v\beta_3 - w\beta_2)/f'(\varepsilon) \\ -2\left[\left(\rho_w \dfrac{\pi d^2}{4} + m_a\right)(\beta_3 U_c - \beta_0 V_c - \beta_1 W_c) + m(w\beta_1 - u\beta_3)\right] \\ 2\left[\left(\rho_w \dfrac{\pi d^2}{4} + m_a\right)(\beta_2 U_c - \beta_1 V_c + \beta_0 W_c) + m(v\beta_1 - u\beta_2)\right] \\ 0 \\ 2(1+\varepsilon)\beta_3 \\ -2(1+\varepsilon)\beta_2 \\ 0 \\ 0 \\ 0 \\ 0 \\ 0 \\ 0 \\ 0 \end{bmatrix}, \qquad (36)$$

$$\mathbf{M}_3 = \begin{bmatrix} 2m(w\beta_3 + v\beta_2)/f'(\varepsilon) \\ 2\left[\left(\rho_w \dfrac{\pi d^2}{4} + m_a\right)(\beta_2 U_c - \beta_1 V_c + \beta_0 W_c) - m(u\beta_2 - w\beta_0)\right] \\ 2\left[\left(\rho_w \dfrac{\pi d^2}{4} + m_a\right)(\beta_3 U_c - \beta_0 V_c - \beta_1 W_c) - m(v\beta_0 + u\beta_3)\right] \\ 0 \\ -2(1+\varepsilon)\beta_2 \\ -2(1+\varepsilon)\beta_3 \\ 0 \\ 0 \\ 0 \\ 0 \\ 0 \\ 0 \\ 0 \end{bmatrix}, \qquad (37)$$

$$\mathbf{M}_4 = \begin{bmatrix} -2m(w\beta_0 + v\beta_1)/f'(\varepsilon) \\ 2\left[\left(\rho_w \dfrac{\pi d^2}{4} + m_a\right)(\beta_1 U_c + \beta_2 V_c + \beta_3 W_c) + m(u\beta_1 + w\beta_3)\right] \\ 2\left[\left(\rho_w \dfrac{\pi d^2}{4} + m_a\right)(\beta_0 U_c + \beta_3 V_c - \beta_2 W_c) + m(u\beta_0 - v\beta_3)\right] \\ 0 \\ 2(1+\varepsilon)\beta_1 \\ 2(1+\varepsilon)\beta_0 \\ 0 \\ 0 \\ 0 \\ 0 \\ 0 \\ 0 \\ 0 \end{bmatrix}, \qquad (38)$$

$$\mathbf{M}_5 = \begin{bmatrix} -2m(w\beta_1 - v\beta_0)/f'(\varepsilon) \\ -2\left[\left(\rho_w \dfrac{\pi d^2}{4} + m_a\right)(\beta_0 U_c + \beta_3 V_c - \beta_2 W_c) + m(u\beta_0 + w\beta_2)\right] \\ 2\left[\left(\rho_w \dfrac{\pi d^2}{4} + m_a\right)(\beta_1 U_c + \beta_2 V_c + \beta_3 W_c) + m(v\beta_2 + u\beta_1)\right] \\ 0 \\ -2(1+\varepsilon)\beta_0 \\ 2(1+\varepsilon)\beta_1 \\ 0 \\ 0 \\ 0 \\ 0 \\ 0 \\ 0 \\ 0 \end{bmatrix}. \qquad (39)$$

The vector **P** is given by

$$\mathbf{P} = \begin{bmatrix} \dfrac{S_b\Omega_2}{f'(\varepsilon)} - \dfrac{S_n\Omega_3}{f'(\varepsilon)} - \dfrac{w_0}{f'(\varepsilon)}(\beta_0^2 + \beta_1^2 - \beta_2^2 - \beta_3^2) - \frac{1}{2}\rho_w d\pi C_{dt}\dfrac{(u-u_c)|u-u_c|}{f'(\varepsilon)}\sqrt{1+\varepsilon} \\ f(\varepsilon)\Omega_3 - S_b\Omega_1 - 2w_0(\beta_1\beta_2 - \beta_0\beta_3) - \frac{1}{2}\rho_w d C_{dp}(v-v_c)\sqrt{(v-v_c)^2+(w-w_c)^2}\sqrt{1+\varepsilon} \\ S_n\Omega_1 - f(\varepsilon)\Omega_2 - 2w_0(\beta_1\beta_3 + \beta_0\beta_2) - \frac{1}{2}\rho_w d C_{dp}(w-w_c)\sqrt{(v-v_c)^2+(w-w_c)^2}\sqrt{1+\varepsilon} \\ \Omega_2 w - \Omega_3 v \\ \Omega_3 u - \Omega_1 w \\ \Omega_1 v - \Omega_2 u \\ \frac{1}{2}(\beta_1\Omega_1 + \beta_2\Omega_2 + \beta_3\Omega_3) \\ -\frac{1}{2}(\beta_0\Omega_1 - \beta_3\Omega_2 + \beta_2\Omega_3) \\ -\frac{1}{2}(\beta_3\Omega_1 + \beta_0\Omega_2 - \beta_1\Omega_3) \\ \frac{1}{2}(\beta_2\Omega_1 - \beta_1\Omega_2 - \beta_0\Omega_3) \\ 0 \\ \left(\dfrac{GI_p}{EI} - 1\right)\Omega_1\Omega_3 - \dfrac{1}{EI}S_b(1+\varepsilon)^3 \\ \left(1 - \dfrac{GI_p}{EI}\right)\Omega_1\Omega_2 + \dfrac{1}{EI}S_n(1+\varepsilon)^3 \end{bmatrix}. \qquad (40)$$